University of Groningen

Spectral Properties of Populations Behind the Coherence in Spitzer Near-infrared and Chandra X-Ray Backgrounds

Li, Yanxia; Cappelluti, Nico; Hasinger, Günther; Arendt, Richard G.; Kashlinsky, Alexander; Pacucci, Fabio

[Link to publication in University of Groningen/UMCG research database](Link)

Spectral Properties of Populations Behind the Coherence in *Spitzer* Near-infrared and *Chandra* X-Ray Backgrounds

Yanxia Li[1], Nico Cappelluti[2] , Günther Hasinger[1,3] , Richard G. Arendt[4,5] , Alexander Kashlinsky[4,6], and Fabio Pacucci[7,8]

[1] Institute for Astronomy, University of Hawaii at Manoa, Honolulu, HI 96822, USA
[2] Physics Department, University of Miami, Coral Gables, FL 33124, USA; ncappelluti@miami.edu
[3] European Space Astronomy Centre (ESA/ESAC), Director of Science, E-28691 Villanueva de la Cañada, Madrid, Spain
[4] Observational Cosmology Laboratory, Code 665, Goddard Space Flight Center, 8800 Greenbelt Road, Greenbelt, MD 20771, USA
[5] CRESST II/University of Maryland, Baltimore County, 1000 Hilltop Circle, Baltimore, MD 21250, USA
[6] SSAI, Lanham, MD 20706, USA
[7] Department of Physics, Yale University, New Haven, CT 06511, USA
[8] Kapteyn Astronomical Institute, Groningen, 9747 AD, Netherlands

Received 2019 January 1; revised 2019 August 6; accepted 2019 August 6; published 2019 September 20

Abstract

We study the coherence of the near-infrared and X-ray background fluctuations and the X-ray spectral properties of the sources producing it. We use data from multiple *Spitzer* and *Chandra* surveys, including the UDS/SXDF surveys, the *Hubble* Deep Field North, the EGS/AEGIS field, the *Chandra* Deep Field South, and the COSMOS surveys, comprising $\sim$2275 *Spitzer*/IRAC hours and $\sim$16 Ms of *Chandra* data collected over a total area of $\sim$1 deg^2. We report an overall $\sim$5σ detection of a cross-power signal on large angular scales >20″ between the 3.6 and 4.5 μm and the X-ray bands, with the IR versus [1–2] keV signal detected at 5.2σ. The [0.5–1] and [2–4] keV bands are correlated with the infrared wavelengths at a $\sim$1–3σ significance level. The hardest X-ray band ([4–7] keV) alone is not significantly correlated with any infrared wavelengths due to poor photon and sampling statistics. We study the X-ray spectral energy distribution of the cross-power signal. We find that its shape is consistent with a variety of source populations of accreting compact objects, such as local unabsorbed active galactic nuclei or high-z absorbed sources. We cannot exclude that the excess fluctuations are produced by more than one population. Because of poor statistics, the current relatively broad photometric bands employed here do not allow distinguishing the exact nature of these compact objects or if a fraction of the fluctuations have instead a local origin.

Key words: cosmology: observations – infrared: diffuse background – quasars: supermassive black holes – X-rays: diffuse background

1. Introduction

Sources presently undetected at any wavelength leave footprints in cosmic backgrounds. In the near-infrared (NIR) photons from the cosmic infrared background (CIB) reveal otherwise undetected star-forming galaxies, active galactic nuclei (AGNs), the Galaxy, and even objects from the reionization epoch that, because of redshift, may peak in the *Spitzer* bands.

Measuring the absolute levels of the CIB suffers from large systematic uncertainties associated with foreground subtraction. Studying CIB fluctuations is a promising alternative because it is much less sensitive to the absolute zero-point of the measurements. In addition, a fluctuation analysis could potentially distinguish undetected components, e.g., early black holes (BHs) and intra halo light (IHL), from known populations of stars, galaxies, and AGN (Kashlinsky et al. 1996). This opens up the possibility of isolating high-z emissions due to the distinct spectral amplitude and structure of the underlying early sources (Cooray et al. 2004; Kashlinsky et al. 2004).

There have been a few studies about the coherence between the cosmic X-ray background (CXB) and the CIB (Cappelluti et al. 2013, 2017; Mitchell-Wynne et al. 2016; Li et al. 2018). These studies mostly focused on the cross-power spectra, which were used to study the possible contributing sources to the cross-power. The observed coherence between CIB and CXB has been explained by BHs, e.g., direct collapse BHs (DCBHs; Yue et al. 2013), which are high-mass ($10^{4-6} M_\odot$)

black hole seeds predicted to form in pristine, high-z environments (Bromm & Loeb 2003), or accreting primordial BHs (PBHs; Kashlinsky 2016; Kashlinsky et al. 2019a), which are stellar-mass objects formed during or after the inflation period. Following these theoretical proposals, Kashlinsky et al. (2005, 2007) identified in deep *Spitzer*-based analysis significant source-subtracted CIB fluctuations at levels much higher than expected from remaining known sources (Helgason et al. 2012, 2014; Kashlinsky et al. 2012). See the recent review by Kashlinsky et al. (2018) for a summary and discussion.

In addition to studying the cross-power spectrum itself, it is also possible to use the spectral energy distribution (SED) of the mean cross-powers as a distinguishing diagnostic of the X-ray spectra of the different source models. In fact, Li et al. (2018) first studied the SED shape of the cross-power signal using COSMOS data only, but found that they cannot effectively discriminate various models due to limitations of the data in their study. Cappelluti et al. (2013, 2017) showed that while the coherence between the CIB and CXB is of the order 10%–20%, this is a strong function of the angular scales, approaching 1 between 20″ and 1000″. Moreover, the coherence between the CIB and the CXB in different subbands is essentially the same (see Li et al. 2018). In this paper we are interested in characterizing the excess power in the 20″–1000″ angular range, and given the considerations listed above we can reasonably assume that the populations responsible for this signal in the CIB versus CXB cross-power are intrinsically highly correlated. This might suggest that the same source

Table 1
X-Ray Map Properties

	UDS	HDFN	EGS	CDFS	COSMOS
# of pointings	25	20	97	101	117
Area (deg^2)	0.12	0.02	0.10	0.04	0.74
Pixel Scale ($''$)	1.2	0.6	1.2	0.6	1.2
$S_{\mathrm{lim},0.5-2\,\mathrm{keV}}$ (cgs)	1.4×10^{-16}	2.5×10^{-17}	2.0×10^{-16}	6.4×10^{-18}	2.2×10^{-16}
$\%_{\mathrm{mask}}$	37.8%	37.5%	31.8%	39.1%	46.6%
$N_{\mathrm{ph},[0.5-1]}^{\mathrm{u}}$	41551	134065	56547	710949	75360
$N_{\mathrm{ph},[0.5-1]}^{\mathrm{m}}$	24084	65207	30539	356632	31628
$N_{\mathrm{ph},[1-2]}^{\mathrm{u}}$	71955	209295	114557	1475705	170025
$N_{\mathrm{ph},[1-2]}^{\mathrm{m}}$	36172	84905	58264	646442	62753
$N_{\mathrm{ph},[2-4]}^{\mathrm{u}}$	100203	255677	168682	2114792	235235
$N_{\mathrm{ph},[2-4]}^{\mathrm{m}}$	56227	136167	105535	1151228	110308
$N_{\mathrm{ph},[4-7]}^{\mathrm{u}}$	132249	302467	192454	2420475	264213
$N_{\mathrm{ph},[4-7]}^{\mathrm{m}}$	78629	176220	126445	1406109	133298

Note. We summarize the X-ray photon counts before masking ($N_{\mathrm{ph}}^{\mathrm{u}}$) and after masking ($N_{\mathrm{ph}}^{\mathrm{m}}$) for each X-ray narrow band, in each field. References for the used catalogs are as follows. UDS: Kocevski et al. (2018), HDFN: Alexander et al. (2003), EGS: Goulding et al. (2012), CDFS: Luo et al. (2017), COSMOS: Civano et al. (2016).

populations produce the observed excess large-scale cross-power. For this reason we can assume that using the amplitude of the cross-power is a tool to estimate the stacked (or average) X-ray spectrum of the unknown sources producing the excess fluctuations. The shape of such an SED can help investigate the nature of these sources. The goal of this paper is to provide the spectrum of these correlated sources, although this work does not provide a definitive distinction between the several source populations proposed to produce this signal.

In this work, for the first time, we combine the data from multiple fields with deep *Spitzer* and *Chandra* data and probe the SED of the CIB–CXB cross-power signal at four narrow X-ray bands: [0.5–1], [1–2], [2–4], and [4–7] keV, in order to study the X-ray spectral properties of the CIB–CXB cross-power.

2. Data Sets and Map Making

2.1. Chandra *X-Ray Data*

We collect and analyze the X-ray data from five surveys: the *Chandra* Legacy Survey of the UKIDSS Ultra Deep Survey Field (UDS; Kocevski et al. 2018), the Hubble Deep Field North (HDFN; Alexander et al. 2003), the *Chandra* ACIS-I AEGIS survey (EGS; Goulding et al. 2012), the *Chandra* Deep Field South (CDFS; Luo et al. 2017), and the *Chandra* COSMOS-Legacy Survey (COSMOS; Civano et al. 2016). Some information about each field is listed in Table 1. These are five of the deepest and most studied fields by both *Chandra* and *Spitzer*. The choice of these fields is also driven by their deep coverage with *HST* to allow future cross-correlation studies with shorter-wavelength optical and NIR data. Following Li et al. (2018), we reduce our data using the *Chandra* Interactive Analysis of Observations software (CIAO; Fruscione et al. 2006) with the main procedures summarized as below. The level = 1 event files are recalibrated and cross-matched with corresponding optical catalogs to further improve the absolute pointing accuracy. We examine the light curves of the background and clean the flares that otherwise could contaminate the real cosmic background signal. The exposure maps are evaluated at a single energy value (middle value of each band) to avoid introducing bias from modeling. Similar

procedures are applied on the stowed data, which were taken when the ACIS detector was out of the focal plane, and these data are used in estimating the particle-only background (Hickox & Markevitch 2006).

We number the X-ray photons sequentially by their arrival time and map them into images "A" (using odd numbered photons) and "B" (using even numbered photons). A and B maps have the same exposure time and have been observed simultaneously so that the difference map of the two (A–B) only contains instrumental effects. We then create the mosaic signal maps (A+B) and noise maps (A–B) to estimate the noise level.

The mosaic maps are created in four narrow bands: [0.5–1], [1–2], [2–4], and [4–7] keV. This combination of bands is the result of a tradeoff between increasing the number of bands and maximizing the signal-to-noise ratio (S/N) per band. The X-ray masks are created by removing any pixels within a $7''$ radius around each point source in the corresponding source catalogs (Table 1). The mask radius is chosen to remove >90% brightness of the detected X-ray sources (Civano et al. 2016). The extended emissions from groups and clusters of galaxies are identified and incorporated in the masks as well (Finoguenov et al. 2010, 2015; Erfanianfar et al. 2013, 2014).

The X-ray maps are matched to the IR maps (Section 2.2), so that they have the same astrometry and pixel scales. The CDFS and HDFN have smaller pixel scales (i.e., $0.''6$ versus $1.''2$) because the deeper coverage of these fields facilitates subpixelization of the data, which allows slightly more detailed source masking. No changes in the large-scale power have been noted between these choices of pixel scale of the final images. Combining the X-ray masks with the corresponding IR masks, we obtain the final masks ($M_{\mathrm{IR,X}}$) for the CIB–CXB cross-power analysis. As shown by Helgason et al. (2014), IR maps are deeper than X-ray maps for typical X-ray sources. This means that even if the depth of the surveys is different in the X-ray band, the maps have very similar shot noise levels as shown by comparing Figures 14 and 17 of Li et al. (2018). The numbers of photons before and after masking in each band are shown in Table 1 together with flux limits of the surveys in the [0.5–2] keV band.

2.2. Spitzer IR Data

Our IR data (3.6 and 4.5 μm) are taken with *Spitzer*/IRAC from multiple programs: the *Spitzer* Extended Deep Survey program (UDS: program ID = 61041, EGS: program ID = 61042; Fazio & SEDS Team 2011), the GOODS Legacy program (HDFN: program ID = 169, CDFS: program ID = 194; Dickinson et al. 2003), and the *Spitzer* Large Area Survey with the HyperSuprime-Cam (COSMOS: program ID = 90042; Steinhardt et al. 2014).

Detailed data reduction is described in Li et al. (2018, and references therein), with the main procedures summarized as below. The reduction starts with the corrected basic calibrated data (cBCD). The data are grouped and processed with the self-calibration method (Arendt et al. 2010), with the model described as $D^i = S^\alpha + F^p + F^q$, where D^i is the measured intensity of a single pixel i from the single frame q, and S^α is the true sky intensity at location α. F^p and F^q describe the offset between the observed and the expected sky intensity, where F^p remains constant with time and records the offset for detector pixel p, while F^q is variable during the observations. The self-calibration helps to remove some artifacts[9] on the images from, e.g., "first-frame effect," which is due to the fact that the detector response is noticeably different before and after long slews when the detector is periodically scanning the field during the course of the observations.

Each field has two mosaic maps at both IR wavelengths created by merging the calibrated frames together. Source detection and masking are done on the mosaic maps with two major steps: (1) source modeling, to identify and remove point sources and resolved extended sources; (2) masking (sigma clipping), to clean up the artifacts from modeling and the remaining emission from bright sources (Arendt et al. 2010).

The source-subtracted CIB fluctuations could be contributed by the shot noise from remaining sources in the beam and the clustering of the remaining CIB sources. The CIB fluctuations are measured at a given shot noise level, $P_{\rm SN} = \int S^2(m)dN(m)$, which we express in units of nJy nW m^{-2} sr^{-1} (see Kashlinsky et al. 2018, Section IV. A.1). The COSMOS maps are clipped to the shot noise level of $\sim$86 nJy nW m^{-2} sr^{-1}, and other maps are at the level of $\sim$50 and $\sim$30 nJy nW m^{-2} sr^{-1} in 3.6 and 4.5 μm, respectively.

3. Fourier Analysis of the Fluctuation Maps

For each field, at each IR and X-ray wavelength, we have the mosaic maps with resolved sources masked out by applying $M_{\rm IR,X}$. We then use the Fourier transforms (via a fast Fourier transfor algorithm) to extract the cross-power spectrum for each possible pair of the IR and X-ray wavelengths.

Following the conventions in Kashlinsky et al. (2012) and Cappelluti et al. (2013), the fluctuation map is defined as

$$\delta F(\boldsymbol{x}) = I(\boldsymbol{x}) - \langle I(\boldsymbol{x}) \rangle, \tag{1}$$

and its 2D Fourier transform is

$$\Delta(\boldsymbol{q}) = \frac{1}{4\pi^2} \int \delta F(\boldsymbol{x}) \exp(-i\boldsymbol{x} \cdot \boldsymbol{q}) d^2x. \tag{2}$$

The autopower spectrum (at a single band) is

$$P(q) = \langle |\Delta(\boldsymbol{q})|^2 \rangle, \tag{3}$$

---

averaged over $[q, q + \delta q]$. The error estimation of $P(q)$ is

$$\sigma_{P(q)} = P(q) \Big/ \sqrt{0.5N_q}, \tag{4}$$

where $0.5N_q$ is the number of independent Fourier elements. The CIB–CXB cross-powers are calculated using

$$P_{1 \times 2}(q) = \langle \Delta_1(q) \Delta_2^*(q) \rangle, \tag{5}$$

with the errors

$$\sigma_{P_{1 \times 2}(q)} = \sqrt{P_1(q)P_2(q)/N_q}. \tag{6}$$

Throughout the paper, we also compute the mean squared fluctuations, which are calculated as $q^2 P(q)/2\pi$ as a function of the angular scales, $2\pi/q$. In order to combine signals, all of the maps from different fields have the same Fourier binning to give power at identical angular frequencies (q).

4. Results

4.1. Cross-power Spectra

The stacked cross-powers are calculated by the simple mean of the powers from the five subfields, instead of weighted averages. Because uncertainties of the cross-powers are derived from the signal, randomly low (or high) measurements are assigned artificially small (or large) uncertainties. Therefore, the weighted averages will be biased toward the lower values and the overall uncertainties could be biased. We calculate the cross-powers between IR maps and the stowed X-ray images (reprojected to the astrometric frame of the IR images) in the same manner and find that the cross-powers are consistent with zero for all pairs as shown in Figure 1. The cross-powers with the stowed X-ray maps are subtracted from the cross-power spectra. The resulting cross-powers are shown in Figure 2.

As demonstrated in Cappelluti et al. (2013, 2017), Mitchell-Wynne et al. (2016), and Li et al. (2018) the CIB versus CXB cross-power is in excess over shot noise at angular scales larger than 20″. Since at those scales known foregrounds are significantly weaker than our signal (Helgason et al. 2014; Cappelluti et al. 2017; Kashlinsky et al. 2018), we therefore calculate the weighted mean cross-power above 20″ as

$$\langle q^2 P_{\rm IR,X} \rangle / \langle q^2 \rangle, \tag{7}$$

between each IR and X-ray band, for each field and for the stacked cross-power spectrum. As shown in Table 2, the [1–2] keV band is significantly correlated with all IR wavelengths at $\sim$5σ significance level, while the [0.5–1] and [2–4] keV bands are correlated with the IR wavelengths at $\sim$1–3σ levels. There is no significant cross-power signal between the [4–7] keV band and any IR wavelengths so we cannot exclude an intrinsic correlation. By including the COSMOS field with a larger area, our new analysis extends the CIB–CXB cross-power analysis to $\sim$3000″, doubling the largest scale reached in Cappelluti et al. (2017). The reason the highest significance is in the [1–2] keV band is due the higher S/N due to the peak in effective area of the *Chandra* mirror in that spectral region. Stacked results in the hard X-ray band (i.e., [2–4] keV + [4+7] keV) are not as significant as in Li et al. (2018) since deep fields add data affected by strong cosmic variance on very large scales. In the hard band most of the events are particles, so the low astrophysical hard X-ray photon statistics is another source of noise. As a cross-check we
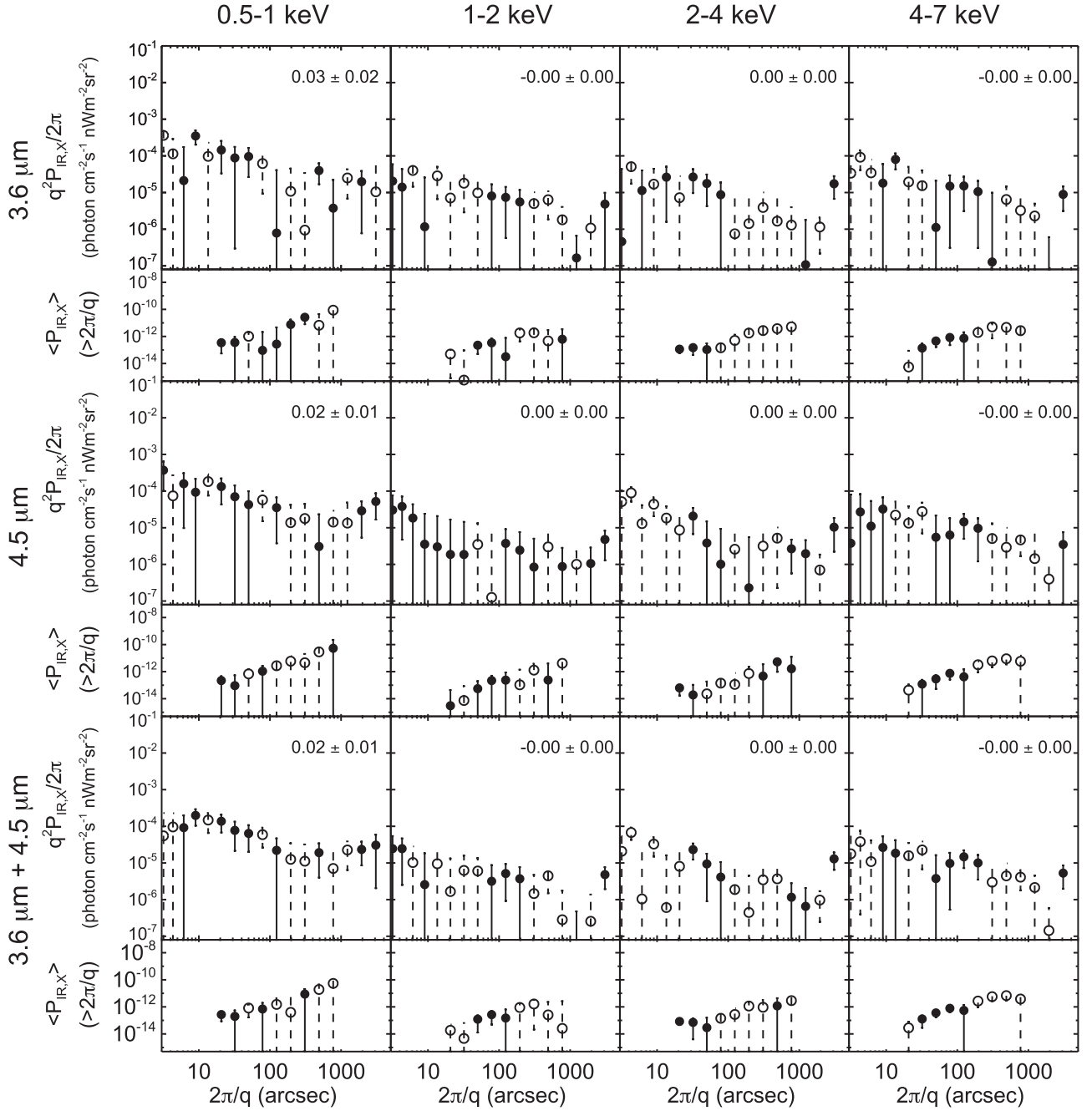
Figure 1. Stacked CIB–stowed background cross-power spectra: between 3.6 μm and [0.5–1], [1–2], [2–4], and [4–7] keV stowed background (upper panels); between 4.5 μm and stowed background (middle panels). Open circles with dashed error bars denote the absolute values of negative results. For completeness we also show the combined 3.6 μm + 4.5 μm vs. stowed background in the bottom panels. In the labels we show the average cross-power above 20″.

compared the significance of our stacks with those shown in Figure 17 of Li et al. (2018) for the [2–7] keV band versus 3.6 and 4.5 μm and found consistent results.

4.2. Cross-power Hardness Ratios

Similar to the X-ray color–color diagram, we look into three hardness ratios for the mean cross -power, which are the equivalent of photometric color indices, following the typical definition (Brunner et al. 2008)

$$HR1 = \frac{\langle P_{IR,[1-2]\ keV}\rangle - \langle P_{IR,[0.5-1]\ keV}\rangle}{\langle P_{IR,[1-2]\ keV}\rangle + \langle P_{IR,[0.5-1]\ keV}\rangle}, \quad (8)$$

$$HR2 = \frac{\langle P_{IR,[2-4]\ keV}\rangle - \langle P_{IR,[1-2]\ keV}\rangle}{\langle P_{IR,[2-4]\ keV}\rangle + \langle P_{IR,[1-2]\ keV}\rangle}, \quad (9)$$

$$HR3 = \frac{\langle P_{IR,[4-7]\ keV}\rangle - \langle P_{IR,[2-4]\ keV}\rangle}{\langle P_{IR,[4-7]\ keV}\rangle + \langle P_{IR,[2-4]\ keV}\rangle}. \quad (10)$$

The statistical 1σ hardness ratio errors are calculated from the mean power (Table 2) by error propagation. The mean 1σ errors for the hardness ratios are $\sim$0.3 for HR1 and HR2 and $\sim$0.8 for HR3. Due to the larger errors in HR3, resulting from the uncertainties from harder bands, we only examine the relations between HR1 and HR2.
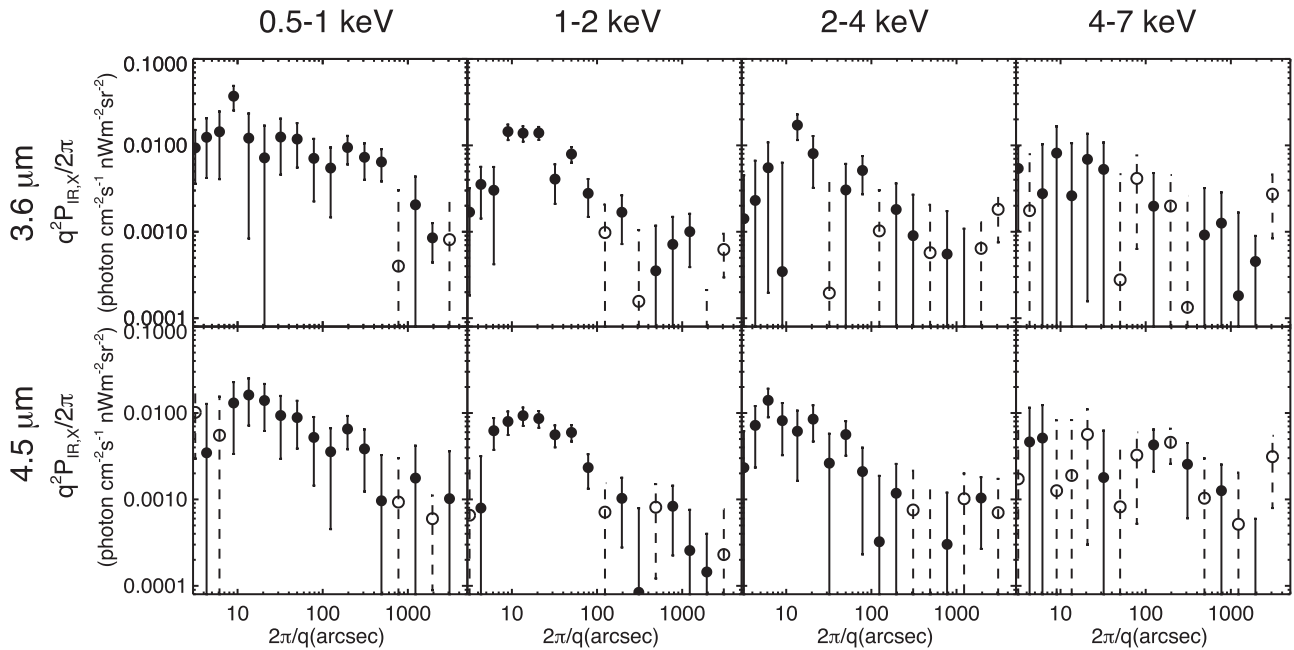
Figure 2. Stacked CIB–CXB cross-power spectra: between 3.6 μm and [0.5–1], [1–2], [2–4], and [4–7] keV (top panels); between 4.5 μm and CXB (bottom panels). Open circles with dashed error bars denote the absolute values of negative results. Note that the shown spectra are subtracted by the cross-power between IR and the stowed X-ray map, that is, the potential contamination from the X-ray particle background is removed from our final results. The final mean powers (used for further SED analysis) are summarized in Table 1.

Figure 3 shows plots of the observed hardness ratios in comparison to various models, with the grid lines referring to single-component models for the X-ray emission. We examine three cases:

(1) Hot gas emissions ($z = 0.5$): a thermal plasma model with Galactic absorption, with the model defined as WABS*A-PEC in XSPEC notation (version 12.10.0; Arnaud 1996). "APEC" is an emission spectrum from collisionally ionized diffuse gas calculated from the AtomDB atomic database.[10] The temperature T ranges from $kT = 0.05$ to 10 keV.

Although a hot gas model with $kT \sim 3$–10 keV at $z = 0.5$ might match the data as shown in Figure 3, it is not physically possible. Such a high temperature probably corresponds to a massive cluster of galaxies, e.g., $10^{14} M_\odot$. By construction, these clusters are actually masked out and their source density is expected to be <1 in our field of view. Cappelluti et al. (2013) have also found that removing X-ray clusters with an extra X-ray mask does not alter the CIB fluctuations, so clusters do not have significant contributions. If the observed X-ray emission is due to hot gas, the temperature should be significantly lower, as adopted in Figure 4. It is worth noticing that an analysis of the XBöotes field by Kolodzig et al. (2017) showed instead that the bulk of large-scale fluctuations in the maps was produced by galaxy clusters and groups in the mass range $10^{13-14} M_\odot$. However, such an analysis was obtained with an average exposure of 5 ks over the field of view. Our stacked results are obtained with an average exposure of ~ 2 Ms. Our observations are on average 400 times deeper than theirs, so the diffuse sources producing the large-scale fluctuations in their observations have been masked here. Therefore, we can safely exclude moderately massive clusters as contributors to the cross-power signal.

(2) A possible alternative is that a missing population of intermediate-redshift AGNs (at $z = 1$–3) could be responsible for the excess. In order to model such a population we approximate its spectrum with a simple absorbed power-law model that accounted for the Galactic hydrogen absorption and a possible intrinsic absorption at the source redshift, with the model defined as WABS*ZWABS*ZPO. Each grid line in Figure 3 (middle column) corresponds to this model spectrum with photon indices $\Gamma = 0, 1, 2, 3$ and intrinsic absorption (in the observer frame) of the Galactic hydrogen column density (N_H) = 10^{21}, 10^{22}, and 10^{23} cm^{-2}. By carefully examining Figure 3, we find that the hardness ratios strongly disfavor a scenario where the bulk of the population is produced by a moderate-redshift, highly obscured AGN population. Our data are instead consistent with a weakly absorbed power law with a spectral index of the order $\Gamma \sim 2$–3, which is rather steep for type 1 AGNs (see, e.g., Just et al. 2007). The mean colors are very soft, and therefore if an absorbed AGN population is present, it would also require an additional softer component that may be associated with star formation.

(3) It has been postulated that a possible population of very high-z AGNs ($z = 10$) in the form of DCBHs could be responsible for the large-scale cross-power. These sources are expected to be extremely Compton thick and show two main peaks in the SED, one at ~ 2–5 μm and another at 1 keV in the observers' frame. These SEDs have been presented in several works (e.g., Yue et al. 2013; Pacucci et al. 2015, 2017, 2018). The X-ray components of these SEDs are shown in Figure 4 folded through the *Chandra* response matrices. However, we also wanted to test the case for unabsorbed high-z AGNs, so we computed hardness ratios with with two types of models. One is a single power law with intrinsic absorption (ZWABS*ZPO, with $\Gamma = 0, 1, 2, 3$ and column density $N_H = 10^{21}$, 10^{22}, and 10^{23} cm^{-2}). The other one is for special Compton-thick sources, whose spectra are dominated by a
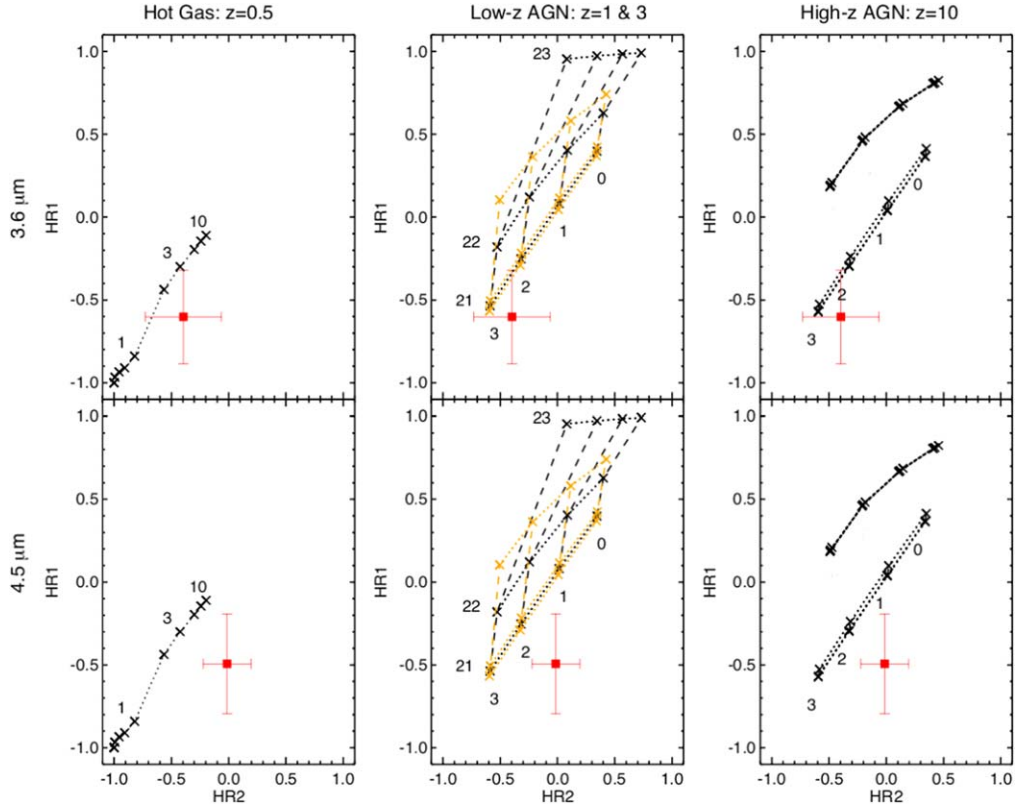
---

[10] http://atomdb.org

Figure 3. Color–color plot or the hardness ratios (HR1 vs. HR2) of $\langle P_{IR,X} \rangle$, with the top row showing HRs using $\langle P_{3.6\,\mu m,X} \rangle$ and the bottom row using $\langle P_{4.5\,\mu m,X} \rangle$. The data point with $\langle P_{IR,X} \rangle$ calculated above $20''$ in each panel (summarized in Table 2) is highlighted with red squares. The error bars represent the 1σ uncertainty on the HR values. We present three cases of the theoretical models for hot gas (left column), AGNs at $z = 1$ and 3 (middle column), and high-z AGNs (right column). The track in the left column shows the Bremsstrahlung spectrum with kT ranging from 0.05 to 10 keV; labels represent the gas temperature. In the middle column, grid lines show the locations of colors for different absorbed power-law spectra. Dashed lines connect spectra with spectral index $\Gamma = 0$–3 as labeled. Dotted lines connect spectra with column densities from $\log(N_H) = 21$ to $\log(N_H) = 23$ as labeled on the left side of the curves. The grid for $z = 3$ is highlighted in orange. In the right column, the upper track (dashed line) is from the PEXRAV model (i.e., a Compton-thick AGN with $N_H = 1.5 \times 10^{24}$ cm^{-2}), with leaking flux (REL_REFL) ranging from 1% to 30% of the total flux, marked from left to right, respectively. The lower double-dotted track is from the simple power-law model at high z with spectral index $\Gamma = 0$–3 as labeled plus galactic absorption. See Section 4.2 for more details about the models.

Table 2
Cross-power Spectrum Amplitude ($>20''$), Calculated as $\langle q^2 P_{IR,X} \rangle / \langle q^2 \rangle$[a]

		[0.5–1] keV	[1–2] keV	[2–4] keV	[4–7] keV
UDS	3.6 μm	1.17 ± 15.61 (0.1σ)	2.07 ± 1.77 (1.2σ)	-1.55 ± 2.80 (-0.6σ)	-2.98 ± 4.11 (-0.7σ)
	4.5 μm	2.90 ± 9.91 (0.3σ)	1.94 ± 1.06 (1.8σ)	1.41 ± 1.74 (0.8σ)	2.29 ± 2.64 (0.9σ)
HDFN	3.6 μm	3.91 ± 3.59 (1.1σ)	1.53 ± 1.28 (1.2σ)	-2.54 ± 2.56 (-1.0σ)	-1.21 ± 3.61 (-0.3σ)
	4.5 μm	1.60 ± 2.85 (0.6σ)	1.50 ± 1.02 (1.5σ)	-2.61 ± 2.06 (-1.3σ)	-1.97 ± 2.86 (-0.7σ)
EGS	3.6 μm	6.07 ± 3.31 (1.8σ)	2.37 ± 1.00 (2.4σ)	1.56 ± 2.12 (0.7σ)	4.01 ± 2.99 (1.3σ)
	4.5 μm	8.57 ± 2.47 (3.5σ)	3.24 ± 0.74 (4.4σ)	1.44 ± 1.56 (0.9σ)	0.11 ± 2.21 (0.0σ)
CDFS	3.6 μm	5.35 ± 2.51 (2.1σ)	3.74 ± 0.61 (6.1σ)	2.54 ± 1.18 (2.2σ)	1.12 ± 1.58 (0.7σ)
	4.5 μm	4.44 ± 2.30 (1.9σ)	2.26 ± 0.58 (3.9σ)	1.88 ± 1.05 (1.8σ)	-3.27 ± 1.38 (-2.4σ)
COSMOS	3.6 μm	20.03 ± 4.86 (4.1σ)	2.87 ± 1.06 (2.7σ)	2.63 ± 2.06 (1.3σ)	1.99 ± 2.93 (0.7σ)
	4.5 μm	8.91 ± 3.76 (2.4σ)	1.78 ± 0.82 (2.2σ)	5.19 ± 1.60 (3.3σ)	2.69 ± 2.26 (1.2σ)
STACK	3.6 μm	10.45 ± 3.12 (3.3σ)	2.60 ± 0.54 (4.8σ)	1.12 ± 1.02 (1.1σ)	0.21 ± 1.45 (0.1σ)
	4.5 μm	6.13 ± 2.18 (2.8σ)	2.08 ± 0.40 (5.2σ)	2.02 ± 0.76 (2.7σ)	0.25 ± 1.09 (0.2σ)

Note.
[a] In units of 10^{-11} photon s^{-1} cm^{-2} nW m^{-2} sr^{-1}.

Compton-reflection continuum from a cold medium, which could be produced by the inner side of the putative obscured torus plus a soft power law and is made by the photons "leaking" through the absorber (Brunner et al. 2008). To reproduce such a spectrum and to compute the expected hardness ratios, we use the XSPEC model PEXRAV, i.e., an exponentially cutoff power-law spectrum reflected from neutral material (Magdziarz & Zdziarski 1995) in a highly obscured environment ($N_H = 1.5 \times 10^{24}$ cm^{-2}), with leaking flux (REL_REFL) ranging from 1% to 30% of the total flux
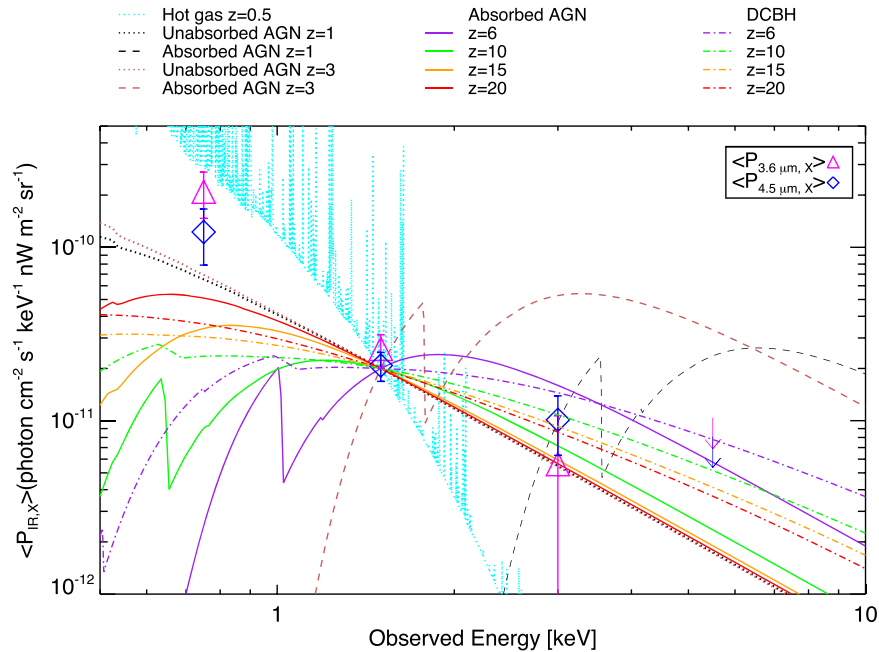
Figure 4. Mean cross-power (calculated above 20″) between 3.6 μm (magenta triangles) or 4.5 μm (blue diamonds) and narrow X-ray bands of [0.5–1], [1–2], [2–4], [4–7] keV as a function of the observed X-ray energy (0.75, 1.5, 3, and 5.5 keV). The 2σ upper limit of the measurement at 5.5 keV is shown as downward arrows. We also show the X-ray spectral models of low-z sources: z = 3 AGNs (dark red), z = 1 AGNs (black), and hot gas (cyan). The absorbed AGNs at z of 6, 10, 15, and 20 are shown in purple, green, orange, and red solid lines, while the DCBH models with the dashed–dotted lines (Section 4.4).

observed. The data appear to be better explained by the single power-law model, although the spectra must be harder than for local AGNs.

4.3. Cross-power SED Modeling

In Figure 4, we present the SED of the mean cross-power. For comparison, we also present X-ray spectral models of absorbed and unabsorbed AGNs, hot gas, and DCBHs. The models for DCBHs are drawn from the radiation-hydrodynamic simulations presented in Pacucci et al. (2015). These simulations require as inputs: (1) initial mass of the seed and (2) initial mass distribution and metallicity of the host galaxy. A typical choice for the initial mass of a DCBH is $\sim 10^5\,M_\odot$, following also the study on the initial mass function of intermediate mass black holes by Ferrara et al. (2014). As the mass increases (within the typical mass range of DCBHs) the normalization of the spectrum increases, with minimal modifications to the overall shape. We can thus interpret the spectral models presented in this paper as typical spectral shapes for DCBHs with an initial mass $\sim 10^5\,M_\odot$. When it comes to the time evolution, typical evolutionary times for these systems are of order 100 Myr. As long as the metallicity and column density do not vary dramatically during the time evolution, the spectral shape undergoes minimal variations, mostly recognizable as modifications of the spectral lines.

The modeled spectra in Figure 4 are rescaled to match the mean levels of the measurements at 1–2 keV. We point out that a quantitative statistical interpretation of the SED is not possible with the current data quality. Hence, the comparison of data with models in this section is qualitative rather than quantitative. In order to examine the implications of the SEDs independent of the results from the hardness ratios, we do not limit our parameter selections to the results from Section 4.2. For AGNs, we assume a simple standard power-law model with two absorption components (WABS*ZWABS*ZPO at

redshifts of z = 1, 3). The first component models the Galactic absorption with a fixed N_H of $1.72 \times 10^{20}\,cm^{-2}$. The second component represents the AGN intrinsic absorption. We choose common values for the power-law photon index ($\Gamma = 1.9$) and N_H ($1.5 \times 10^{24}\,cm^{-2}$ for absorbed AGNs, $10^{21}\,cm^{-2}$ for unabsorbed AGNs; see, e.g., Caccianiga et al. 2004). For the hot gas (Bremsstrahlung spectrum), we use XSPEC model (WABS*APEC) with $kT = 0.5$ keV, at z = 0.5. The predictions for the SEDs of AGNs and DCBHs are computed in the high-redshift domain, at z = 6, 10, 15, 20. The SEDs of the DCBH models specifically tuned to the measured CIB fluctuations can also be found in Yue et al. (2013).

4.4. Data versus SED Model Comparisons

Interpreting the cross-powers, $\langle P\_IR, X\rangle$, shown in Figure 4 as the SED of the correlated X-ray background is consistent (within uncertainties), whether the 3.6 or 4.5 μm cross-power is examined. By comparing the measurements to the models both using the SEDs and hardness ratios, we rule out the possibilities of low-z absorbed AGNs and hot $kT > 3$ keV gas for reproducing our measurements. The other models at high z (absorbed AGNs and DCBHs) appear to fit the data, but they cannot be differentiated due to the negligible difference in their shapes. The differences between absorbed AGNs and DCBHs visible in Figure 4 are mostly due to the presence of metal features in the former class of spectra, while in the latter class the assumption is that the absorbing gas is pristine. There is an indication of an excess at the softest [0.5–1] keV band, which cannot be fully accounted for by any of the models. This might suggest that at softest energy a thermal Galactic component might correlate with residual Galactic cirrus. The most likely spectral shape for the correlating components is either a steep power law or an AGN-like power law plus a very soft thermal component. Our main conclusion is that by using spectral analysis alone we can affirm that, above 1 keV, the spectrum of

primary sources producing CXB fluctuations correlating with the CIB is a power law, which consistent with radiation produced by accretion. At lower energies we see an indication of an excess signal over such a power law, so we cannot exclude a thermal origin of the spectrum pointing to either a Galactic component or to very low mass virialized sources (i.e., groups). In fact, Cappelluti et al. (2013) showed that the main contributors to the large-scale CXB in the CDFS are galaxy groups. However, the contribution of these sources to the CIB is still the subject of investigation, since while emission from IHL (Cooray et al. 2012) has been proposed as a major contributor to the CIB it is not clear if IHL can account for the cross-correlation with the X-rays. On the other hand Cappelluti et al. (2018) proposed that a possible contributor to the cross-power is scattering of X-ray light on galaxy dust, but a recent work by Ricarte et al. (2019) shows that this effect is subdominant. Therefore, through spectral analysis we have evidence that at least part of the sources producing our detected signal are compact accreting objects. However, spectral information is not detailed enough to determine their redshift and detailed population properties.

5. Summary

In order to explain the measured cross-power between CIB and CXB fluctuations, we analyze currently available data sets from multiple fields and make calculations with stacking techniques. We find that the CIB is most significantly correlated with the [1–2] keV background at a ~5σ level. Other bands are correlated at lower significance, but overall we detect a signal whose significance stays constantly above 5σ when adding harder energy bands to the [0.5–1] keV.

In addition, mimicking the studies of X-ray colors using the count rates in different X-ray bands, we visualize the hardness ratios using the mean cross-power. We find that a power-law model, consistent with local accreting unabsorbed AGNs or high-z absorbed AGNs are favored if the sources are accreting compact objects. Local absorbed AGNs and hot $kT > 3$ keV gas are not consistent with our data. Finally, we compare the measured SED of the cross-powers with various models, and we find that unabsorbed AGNs and BHs (AGNs and DCBHs) at high z (>15) can explain the measurements better than other scenarios. We see a deviation from the power-law model at very soft energies suggesting a possible Galactic contamination of the signal. However, with only four X-ray bands over a large range of energies, it is difficult to distinguish what kind of compact source is producing the signal.

Further improvements in the data quality, especially at even larger angular scales from both the IR and the X-ray (Kashlinsky et al. 2019b, 2019c), are needed to explain the origin of the excess cross-power fluctuations. Some other techniques, e.g., Lyman tomography (Kashlinsky et al. 2015), could help to pin down the exact redshift of the source populations.

ORCID iDs

Nico Cappelluti ◉ https://orcid.org/0000-0002-1697-186X
Günther Hasinger ◉ https://orcid.org/0000-0002-0797-0646
Richard G. Arendt ◉ https://orcid.org/0000-0001-8403-8548
Fabio Pacucci ◉ https://orcid.org/0000-0001-9879-7780

References

Alexander, D. M., Bauer, F. E., Brandt, W. N., et al. 2003, AJ, 126, 539
Arendt, R. G., Kashlinsky, A., Moseley, S. H., & Mather, J. 2010, ApJS, 186, 10
Arnaud, K. A. 1996, in ASP Conf. Ser. 101, Astronomical Data Analysis Software and Systems V, ed. G. H. Jacoby & J. Barnes (San Francisco, CA: ASP), 17
Bromm, V., & Loeb, A. 2003, ApJ, 596, 34
Brunner, H., Cappelluti, N., Hasinger, G., et al. 2008, A&A, 479, 283
Caccianiga, A., Severgnini, P., Braito, V., et al. 2004, A&A, 416, 901
Cappelluti, N., Arendt, R., Kashlinsky, A., et al. 2017, ApJL, 847, L11
Cappelluti, N., Bulbul, E., Foster, A., et al. 2018, ApJ, 854, 179
Cappelluti, N., Kashlinsky, A., Arendt, R. G., et al. 2013, ApJ, 769, 68
Civano, F., Marchesi, S., Comastri, A., et al. 2016, ApJ, 819, 62
Cooray, A., Bock, J. J., Keatin, B., Lange, A. E., & Matsumoto, T. 2004, ApJ, 606, 611
Cooray, A., Smidt, J., de Bernardis, F., et al. 2012, Natur, 490, 514
Dickinson, M., Giavalisco, M. & GOODS Team 2003, in The Mass of Galaxies at Low and High Redshift, ed. R. Bender & A. Renzini (Berlin: Springer), 324
Erfanianfar, G., Finoguenov, A., Tanaka, M., et al. 2013, ApJ, 765, 117
Erfanianfar, G., Popesso, P., Finoguenov, A., et al. 2014, MNRAS, 445, 2725
Fazio, G. G. & SEDS Team 2011, in ASP Conf. Ser. 446, Galaxy Evolution: Infrared to Millimeter Wavelength Perspective, ed. W. Wang et al. (San Francisco, CA: ASP), 347
Ferrara, A., Salvadori, S., Yue, B., & Schleicher, D. 2014, MNRAS, 443, 2410
Finoguenov, A., Tanaka, M., Cooper, M., et al. 2015, A&A, 576, A130
Finoguenov, A., Watson, M. G., Tanaka, M., et al. 2010, MNRAS, 403, 2063
Fruscione, A., McDowell, J. C., Allen, G. E., et al. 2006, Proc. SPIE, 6270, 62701V
Goulding, A. D., Forman, W. R., Hickox, R. C., et al. 2012, ApJS, 202, 6
Helgason, K., Cappelluti, N., Hasinger, G., Kashlinsky, A., & Ricotti, M. 2014, ApJ, 785, 38
Helgason, K., Ricotti, M., & Kashlinsky, A. 2012, ApJ, 752, 113
Hickox, R. C., & Markevitch, M. 2006, ApJ, 645, 95
Just, D. W., Brandt, W. N., Shemmer, O., et al. 2007, ApJ, 665, 1004
Kashlinsky, A. 2016, ApJL, 823, L25
Kashlinsky, A., Ali-Haïmoud, Y., Clesse, S., et al. 2019a, BAAS, 51, 51
Kashlinsky, A., Arendt, R., Gardner, J. P., Mather, J. C., & Moseley, S. H. 2004, ApJ, 608, 1
Kashlinsky, A., Arendt, R. G., Ashby, M., et al. 2019b, BAAS, 51, 37
Kashlinsky, A., Arendt, R. G., Ashby, M. L. N., et al. 2012, ApJ, 753, 63
Kashlinsky, A., Arendt, R. G., Atrio-Barandela, F., et al. 2018, RvMP, 90, 025006
Kashlinsky, A., Arendt, R. G., Cappelluti, N., et al. 2019c, ApJL, 871, L6
Kashlinsky, A., Arendt, R. G., Mather, J., & Moseley, S. H. 2005, Natur, 438, 45
Kashlinsky, A., Arendt, R. G., Mather, J., & Moseley, S. H. 2007, ApJL, 654, L5
Kashlinsky, A., Mather, J. C., Helgason, K., et al. 2015, ApJ, 804, 99
Kashlinsky, A., Mather, J. C., Odenwald, S., & Hauser, M. G. 1996, ApJ, 470, 681
Kocevski, D. D., Hasinger, G., Brightman, M., et al. 2018, ApJS, 236, 48
Kolodzig, A., Gilfanov, M., Hütsi, G., & Sunyaev, R. 2017, MNRAS, 466, 3035
Li, Y., Cappelluti, N., Arendt, R. G., et al. 2018, ApJ, 864, 141
Luo, B., Brandt, W. N., Xue, Y. Q., et al. 2017, ApJS, 228, 2
Magdziarz, P., & Zdziarski, A. A. 1995, MNRAS, 273, 837
Mitchell-Wynne, K., Cooray, A., Xue, Y., et al. 2016, ApJ, 832, 104
Pacucci, F., Ferrara, A., Volonteri, M., & Dubus, G. 2015, MNRAS, 454, 3771
Pacucci, F., Loeb, A., Mezcua, M., & Martín-Navarro, I. 2018, ApJL, 864, L6
Pacucci, F., Natarajan, P., Volonteri, M., Cappelluti, N., & Urry, C. M. 2017, ApJL, 850, L42
Ricarte, A., Pacucci, F., Cappelluti, N., & Natarajan, P. 2019, arXiv:1907.03675
Steinhardt, C. L., Speagle, J. S., Capak, P., et al. 2014, ApJL, 791, L25
Yue, B., Ferrara, A., Salvaterra, R., Xu, Y., & Chen, X. 2013, MNRAS, 433, 1556